Atomistic simulation of displacement damage and effective nonionizing energy loss in InAs

Nanjun Chen,[1] Danhong Huang,[2] Eric R. Heller,[3] David A. Cardimona,[2] and Fei Gao[1,*]

[1]*Department of Nuclear Engineering and Radiological Sciences, University of Michigan, Ann Arbor, Michigan 48109, USA*

[2]*U.S. Air Force Research Laboratory, Space Vehicles Directorate, Kirtland Air Force Base, New Mexico 87117, USA*

[3]*U.S. Air Force Research Laboratory, Materials and Manufacturing Directorate, Wright Patterson Air Force Base, Ohio 45433, USA*

(Received 1 August 2019; revised 12 January 2021; accepted 17 February 2021; published 10 March 2021)

A molecular dynamics (MD) method, along with the analytical bond-order potential, is applied to study defect production in InAs. This potential is modified to obtain a better description for point-defect properties and is extended for proper applications in radiation damage simulation. By using this modified potential, the threshold displacement energy (E_d), as one of the crucial parameters in radiation damage studies, is calculated over thousands of crystallographic directions for incorporating spatial anisotropy. However, the E_d dependence on directions is found to be relatively weak. The defect production, clustering, and evolution in InAs are further investigated for the energies of the primary knock-on atom (PKA) ranging from 500 eV to 40 keV. A nonlinear defect production is seen with increasing PKA energy. This nonlinearity, which is associated with the direct-impact amorphization, is very distinctive for PKA energies ranging from 1 to 20 keV. Based on the damage density evaluated from molecular dynamics simulations, a theoretical model is developed for determining nonionizing energy loss (NIEL), which can be used for quantifying the electronic device degradation in a space radiation environment. The NIELs of InAs for proton, alpha, and Xe particles are calculated from the displacement threshold up to 60 MeV in comparison with available data so as to validate our model in the current study.

DOI: 10.1103/PhysRevMaterials.5.033603

I. INTRODUCTION

The use of crystalline semiconductors for detectors and electronic devices operating in high-radiation environments, e.g., particle colliders, space applications, medicine, and industry, makes it necessary to develop radiation resistant materials. The III-V compound semiconductors, such as indium arsenide (InAs), are one of the possible competitors for silicon in different electronic devices. The application of InAs has been widely recognized in spintronic devices, laser diodes, and infrared detectors due to its high electron mobility [1,2] and narrow energy band gap [3]. For example, work done by Balaghi *et al.* [4] has shown the benefit of including InAs in a hybrid III-V compound to the design of high-mobility transistors. With the consideration of avoiding a bulky and costly cryogenic cooling system, the ability of InAs to operate at room temperature could be a primary advantage in space application over other narrow band gap III-V detectors [5]. InAs has also demonstrated superior transient transport properties and strong velocity overshoot phenomena due to the small Γ-valley effective mass of electrons but relatively wide Γ-*L* intervalley separation. This characteristic has been applied to fast and high-frequency electronic devices. However, the damage generated, e.g., point defects and defect clusters, is inevitable during device growth, processing, and space missions, which deteriorates optical and electronic properties. Such damage may result from lattice mismatch, ion-enhanced dry etching for creating nanoscale features, and accurate pattern transfer or bombardment by high-energy ions from the space environment. Electronic devices can be exposed to a high flux of proton, alpha, and heavier ions in a space radiation environment. These charged particles cause radiation damage which degrades the electrical and optoelectronic performance of many devices and becomes a limiting factor for InAs on interplanetary missions. In order to maintain their reliable performance in space, these devices must tolerate the radiation environment of Earth's Van Allen belts [6]. Therefore, a full physics understanding of defect production, stabilization, clustering, migration, and interaction with microstructural imperfections in compound semiconductors becomes a crucial aspect in developing a multiscale theory to explore radiation degradation of electronic and optoelectronic devices.

Practically, a rate of degradation in electronic and optoelectronic devices is described by the number of generated defects in host materials, but experimentally, device degradations are represented by a nonionizing energy loss (NIEL) which is assumed proportional to the number of defects produced by irradiation. As NIEL is capable of providing important guidance in quantifying displacement damage and in correlating the rate of the particle's energy loss with the production of atomic displacements, several theoretical models have been proposed for calculating NIEL, such as the model [7–9] which used the damage code Transport of Ions in Matter (TRIM) [10]. Instead, we introduce and demonstrate a unique type of energy partition function to elucidate physically the displacement-damage effect which is proportional to the NIEL of the primary knock-on atom (PKA) as well as the

*gaofeium@umich.edu

subsequent secondary recoils. This approach has already been applied successfully to GaAs [11] and GaN [12]. Our current model cooperates with the direct information from molecular dynamics (MD) simulations, which capture the recombination process and nonlinear effects. Our theory can predict accurately the effective NIEL, which is not applicable in other Kinchin-Pease based models [13] and, therefore, overcomes the discrepancies between the experiment data and computation results.

In this work we present an extensive computational approach, involving molecular dynamics, to study threshold displacement energy (E_d) dependence on crystallographic orientations in InAs, with an average of over 3600 recoil directions. The statistical results from this simulation are then applied to calculating radiation damage. The defect production, morphology, and clustering in InAs are analyzed quantitatively, as well as the effective nonionizing energy loss, by applying the model developed in previous work [11,12] based on atomic-level knowledge. We demonstrate the significance and robustness of the current approach in understanding how InAs narrow band gap semiconductor materials respond to a severe radiation environment.

II. SIMULATION METHOD

A. Molecular dynamics approach

Simulations were all performed by the MD code MOLDY [14], which was originally developed for simulating displacement cascades in metals [15,16], but the code has been also modified for simulating displacement cascades in compound semiconductors, such as InAs. We have modified the code to construct a zinc-blende structure for a compound semiconductor and atomic interactions based on the formulas detailed in Sec. II B to address three-body contribution and angularity.

For the threshold displacement energy calculation, a simulation box with a size of $10 \times 10 \times 10$ unit cells (consisting of 8000 atoms) was used with a zinc-blende structure for InAs. Periodic boundary conditions were applied to the system. To study threshold displacement energy, E_d, the computational block was equilibrated at 0 K for 5 ps prior to launching a recoil event. To simulate a recoil event, the PKA was given an initial kinetic energy (starting from 6 eV) along a specific crystallographic direction and the dynamic process was evolved for 5 ps afterwards. If the amount of initial energy is enough to overcome the E_d, the PKA will displace from its original site to form a stable interstitial or anion antisite at the end of the simulation. If the crystal remains perfect, on the other hand, the initial kinetic energy will then increase by 2 eV.

Additionally, to simulate a displacement cascade in InAs, a large cell is required. The principle for selecting different cells is to avoid overlap of a displacement cascade with itself due to the periodic condition and, thus, the size varies by different PKA energies. For example, a crystal of 140 608 atoms ($26 \times 26 \times 26$ unit cells) is employed to start a 20 keV PKA to generate a displacement cascade. A variable time step was employed to allow for a small value early in the ballistic phase and for a large value when the energy exchange between atoms declined to thermal levels (general from 0.0001 to 1 fs). To perform a cascade simulation, there are three major steps. First, the system is first heated to 100 K to imitate the thermal energy just above zero-point value allowing equilibration for 10 ps at 100 K to achieve an equilibrium phonon state. Second, a cascade is introduced by a PKA along a randomly selected direction with a kinetic energy ranging from 500 eV to 40 keV. Third, the evolution of a cascade following the primary recoil event is evolved for about 20 ps until there is no significant change in both defect quantity and major migration of defects. In this study, the cascade simulation only specifies for In PKA events, but it can also be extended to As PKAs. To obtain good statistics, 20 PKA events are carried out for each energy in various crystallographic directions. For atomic structure analysis, the Wigner-Seitz (WS) cell first proposed by Wigner and Seitz [17] is used as an examination criterion to identify vacancies, interstitials, and antisite defects by the occupancy of a WS cell of each lattice site. More specifically, the lattice sites with empty Wigner-Seitz cells were labeled as vacancies, and sites occupied by multiple atoms were labeled as interstitials. If an atom occupies a site which was previously occupied by another atom type, an antisite defect was defined. This method has been widely used [18–20] in atomic-level simulations associated with defects and defect production. It should be noted that neither electronic stopping nor ionization has been considered in the simulation due to the lack of a good model to address the ionizing energy loss in classical MD simulation. Therefore, the current simulation might overestimate the defect production at high energies, where electronic stopping takes part.

B. Interatomic potential

The interactions between two atoms are constructed based on an analytic bond-order potential (ABOP), which was proposed by Albe *et al.* [21] and applied extensively to simulate defect properties and defect creation in numerous semiconductors.

The total energy can be written as a sum of individual bond energies, i.e.,

$$V_{\text{tot}} = \sum_{i,j} V_{ij} = \frac{1}{2} \sum_{i,j} f_C(r_{ij})[V_R(r_{ij}) - b_{ij} V_A(r_{ij})]. \quad (1)$$

In the equation, the pairwise repulsive and attractive contributions are given by physically instructive Morse-like structures [22],

$$V_R(r_{ij}) = \frac{D_0}{S-1} \exp[-\beta\sqrt{2S}(r - r_0)], \quad (2)$$

$$V_A(r_{ij}) = \frac{SD_0}{S-1} \exp[-\beta\sqrt{2/S}(r - r_0)], \quad (3)$$

where D_0 is dimer binding energy and r_0 is equilibrium bond length. The cutoff function $f(r_{ij})$ is necessary and computationally efficient to restrict the interaction to the first nearest neighbor. It can be defined as

$$f(r_{ij}) = \begin{cases} 1, & r < R - D \\ \frac{1}{2} - \frac{1}{2} \sin\left(\frac{\pi}{2} \frac{(r-R)}{D}\right), & |R - r| \leqslant D, \\ 0, & R + D < r \end{cases} \quad (4)$$

In the formula, R and D specify the cutoff region; they depend on the type of atoms i, j. Moreover, the bond order potential also contains three-body contribution and angularity, which are given by

$$b_{ij} = (1 + \chi_{ij})^{-1/2}, \tag{5}$$

where

$$\chi_{ij} = \sum_{k(\neq i,j)} f(r_{ik}) \exp[\alpha_{ijk}(r_{ij} - r_{ik})] g(\theta_{ijk}). \tag{6}$$

Then, the angular function in Eq. (6) can be written as

$$g(\theta_{ijk}) = \gamma\left(1 + \frac{c^2}{d^2} - \frac{c^2}{d^2 + [h + \cos\theta]^2}\right). \tag{7}$$

The three-body interactions can be formally determined by five adjustable parameters α, γ, c, d, and h. The interactions between In-In and As-As atoms are described by Hammerschmidt *et al.* [23]. However, the In-As interaction is refitted to ensure a more accurate description for point-defect properties as compared with *ab initio* calculations [24–26] (see Table SII in the Supplemental Material [27]). A reference database which includes elastic moduli and structural properties from experiment [28] and theory [23] is provided in Table SI [27]. The fitting process was performed with the assistance of MATLAB and large-scale atomic/molecular massively parallel simulator (LAMMPS) [29] to achieve parameter optimization based on the Levenberg-Marquardt minimization algorithm [30] with an objective function [31]. The description of this process is detailed in the Supplemental Material [27]. Quantitatively, the fitted potentials alone still cannot give rise to a satisfactory description for short-range interactions which are, however, very important for simulating atomic displacement and defect creation at high recoil energies. To overcome this deficiency, additional modification has been made to these potentials by adding another repulsive potential, i.e., Ziegler-Biersack-Littmark (ZBL) screen potential [32], which describes the high-energy scattering of atoms in solids very well. Specifically, this correction is achieved by combining the ABOP in Eq. (1) with a short-range function through the use of a Fermi-type weight function,

$$F(r) = \frac{1}{1 + e^{-b_f(r - r_f)}}, \tag{8}$$

where $F(r)$ quickly goes to unity as $r \gg r_f$. As a result, the total potential becomes an average connecting the ABOP to the ZBL potential, i.e.,

$$V(r) = V_{\mathrm{ZBL}}[1 - F(r)] + V_{\mathrm{BOP}}F(r), \tag{9}$$

which correctly reduces to the repulsive ZBL potential for small r values and quickly approaches the ABOP for large r values at the same time. The fitting parameters, b_f and r_f, are adjusted to allow for smooth transitions of both total potential and its first derivative. The values of b_f are determined as 14, 14, and 8.5 Å^{-1} for In-In, In-As, and As-As interactions, respectively, while those of r_f are 0.95, 0.75, and 0.85 Å. With the addition of the short-range interaction, we have used the fitted potential to recheck the basic properties of defects. As expected, the results show no difference after the modification. These verifications thus make it appropriate for further displacement cascades study in InAs.

C. NIEL model

In light of the significance of NIEL in understanding the displacement damage of various materials, a theoretical model was developed based on the Lindhard energy-partition function to determine NIEL [33]. Similar to calculating the number of defects, N_F, by PKA in a simplified Kinchin-Pease (KP) model, the displacement damage is found proportional to the kinetic energy of recoils T. Therefore, based on the Lindhard energy-partition function $L(T)$ along with the KP model, NIEL can be written as

$$\mathrm{NIEL} = \beta \int_{E_d}^{T_{\max}} dT\ E(T)L(T)\sigma(T)\,, \tag{10}$$

where β is the atomic density of the target material, and $T_{\max}$ represents the maximum energy that can be transferred to a recoil nucleus by an incident particle. The threshold displacement energy E_d is conventionally taken as 25 eV, but this is not applicable for InAs. The average threshold displacement energy with respect to all orientations in InAs is 15 eV, which will be thoroughly discussed in the next section. $L(T)$ in Eq. (10) is in the simple form of an energy-partition function and the detail can be found in [11]. When the PKA recoil energy E_{PKA} is low, it approximately equals T. When E_{PKA} is high, however, it mostly contributes to the ionization of atoms. In addition, we have $E(T) = E_d N_F/0.4$ from the KP model.

The differential interaction cross section $\sigma(T)$ has been introduced by the ZBL screened formalism for including high-energy scattering of atoms in solids [7].

$$\sigma(T) = \frac{d\delta}{dt} = \frac{-\pi a_U^2}{2}\frac{f(t^{1/2})}{t^{3/2}}, \tag{11}$$

where $t = \varepsilon^2 T/T_{\max}$ is a dimensionless collision parameter related to recoil energy T. $T_{\max}$ is the maximum transferred energy in a collision between an incident ion of mass M_1 and a targeted atom mass of M_2. Here, subscripts 1 and 2 refer to source particles (i.e., proton, alpha, and Xe particle) and targeted atoms (or PKA atoms), respectively.

$$T_{\max} = \frac{4M_1M_2}{(M_1 + M_2)^2}T. \tag{12}$$

ε is the ZBL reduced energy and a_U is the ZBL universal screening length. The parameterized function $f(t^{1/2})$ is referred to as the Thomas-Fermi scattering function.

$$\varepsilon = \frac{32.53M_2E_0}{Z_1Z_2(M_1 + M_2)\left(Z_1^{0.23} + Z_2^{0.23}\right)}, \tag{13}$$

where a_0 is the Bohr radius of the hydrogen atom. Z_1 and Z_2 stand for the atomic numbers of the incident ion and the targeted atom, respectively. In Eq. (13), E_0 indicates the incident energy in keV.

$$a_U = \frac{0.8854a_0}{\left(Z_1^{0.23} + Z_2^{0.23}\right)}, \tag{14}$$

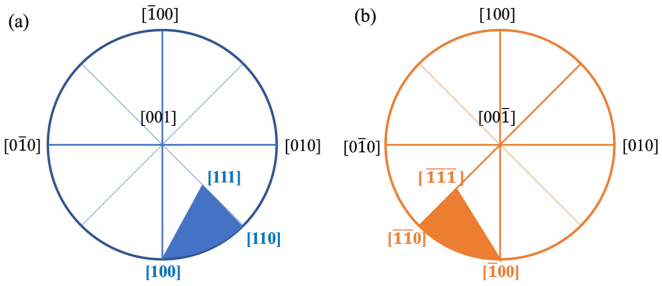

FIG. 1. Illustration of stereographic projections. (a) Positive triangle formed by [100-110-111] on (001) pole; (b) negative triangle formed by [$\bar{1}$00-$\bar{1}\bar{1}$0-$\bar{1}\bar{1}\bar{1}$] on (00$\bar{1}$) pole.

However, the displacement damage associated with the formation of multiple disordered regions or amorphous pockets gives rise to a nonlinear behavior of defect generation. The model in Eq. (10) has its deficiency when using the number of defects provided by a simplified KP model, because the nonlinear behavior has been neglected. Therefore, we improve the accuracy of this NIEL model by obtaining the number density of defects directly from MD simulation to overcome the inaccuracy of the KP model. Our enhanced model has been applied successfully to GaAs [11] and GaN [12]. In MD simulation, the nonlinear process can be fully included. Here, the "effective NIEL," depending on the number of defects simulated by the MD method, becomes

$$\mathrm{NIEL} = \beta \int_{E_d}^{T_{\max}} E^{\mathrm{MD}}(T) L(T) \sigma(T) dT, \tag{15}$$

where $E^{\mathrm{MD}}(T) = E_d N_F^{\mathrm{MD}}(T)/0.4$ and $N_F^{\mathrm{MD}}(T)$, which is the number of defects produced at a given recoil energy T, is calculated from MD simulations to replace N_F in the KP model.

III. RESULTS AND DISCUSSION

A. Threshold displacement energy

Threshold displacement energy is a key parameter to estimate the radiation damage level. It is usually defined as the minimum kinetic energy transferred by PKA to a lattice atom in target material generating at least one stable Frenkel pair. Typically, threshold energy acquires a strong directional anisotropy in crystal materials. For a pure element, a standard unit stereographic triangle contains all the nonequivalent directions for knock-on [34]. However, for a compound semiconductor with zinc-blende structure, e.g., InAs, two triangles are required to investigate the displacement threshold energy for each atom type. Here, one triangle needs three sides of [100-110-111], but another one is associated with the three sides of [$\bar{1}$00-$\bar{1}\bar{1}$0-$\bar{1}\bar{1}\bar{1}$]. To clarify the nomenclature, crystallographic directions on the sides of [100-110-111] are taken as "positive," while directions on the sides of [$\bar{1}$00-$\bar{1}\bar{1}$0-$\bar{1}\bar{1}\bar{1}$] are marked as "negative." The employed crystallographic geometry, which is introduced based on previous work [35] by using the Mercator method, is illustrated in Fig. 1. Two displayed spheres correspond to the zinc-blend structure, where the points on the sphere represent the direction projections. As a whole, more than 1800 directions are simulated for both species taken as a PKA and indicated by two triangles in the Mercator map in this work with a total of 3656 events simulated.

The results of E_d on the sides of the unit triangles for both In and As recoil atoms are shown in Figs. 2(a) and 2(b), respectively. The energy required to create a stable Frenkel pair is in the range of 8–26 eV. The recoils along [100-110] and [$\bar{1}$00-$\bar{1}\bar{1}$0] are clearly equivalent in their orientation dependence on E_d for both atom types. However, the As recoil atom is slightly more sensitive to the chosen directions as compared with the In atom, especially on the sides of [110-111]. The results in Fig. 2(b) reveal a big gap between positive and negative directions for As atoms. The feature of the notably larger values of E_d in negative directions than in positive ones for the recoil events is different from the case of As recoils in GaAs [35]. This may be due to the size discrepancy of the As atom compared to other atom types in materials, since energy transfer efficiency of the lighter PKA to a heavier atom is a dominant factor. In fact, a Ga atom is 1.07 times lighter than As in GaAs, while In is 1.53 times heavier than As in InAs. Consequently, when a recoil event is initiated by an As atom along the [$\bar{1}\bar{1}\bar{1}$] direction, the generation of the stable displacement without recombination needs a larger E_d. This explanation also applies to different features of Ga and In atoms corresponding to the directions on the sides of [110-111], where the difference in the negative and positive directions for an In atom was not so significant. The other important feature accounting for the anisotropy of E_d is the large difference along the directions on the sides of [111-100] and [$\bar{1}\bar{1}\bar{1}$-$\bar{1}$00]. For this case, higher E_d in the negative directions for As is observed, which is similar to In recoils in positive directions. This can be attributed to the strong repulsive energy between As atoms as well as between its first nearest neighbor In atom and vice versa, forcing the kickback to its equilibrium site during a collision or a PKA trajectory shifting. The mismatch of the direction dependence of E_d in positive and negative directions appears exclusively in the compound semiconductor, while in monatomic diamond structured semiconductors (e.g., Si), E_d is equivalent in all ⟨111⟩ directions [36]. One other noticeable feature is that the minimum value which corresponds to channeling directions is not only observed in the low-index direction but also noticeable in the intermediate direction. This result coincidences with the observation in ion channeling effects in gold nanocluster under He ion irradiation [37].

To unveil the mystery of the direction dependence of E_d, a large number of crystallographic directions within the stereographic projection triangles are also taken into account as a function of angles. Each point within the triangles stands for a direction projection. There are more than three thousand recoil events in total performed to get a smooth and comprehensive distribution, and an in-depth understanding of E_d dependence on crystallographic orientation. Figures 3(a) and 3(b) present the contour map of the three-dimensional threshold displacement energy surface obtained from the simulations for In and As recoils, respectively, where different colors correspond to various energy scales. We noticed that both In and As atoms can stay at the lowest energy, 8 eV, to knock off a neighbor atom and produce a persistent defect along a given direction. An interesting observation lies between the energy surfaces in the positive triangle of In and the negative triangle of

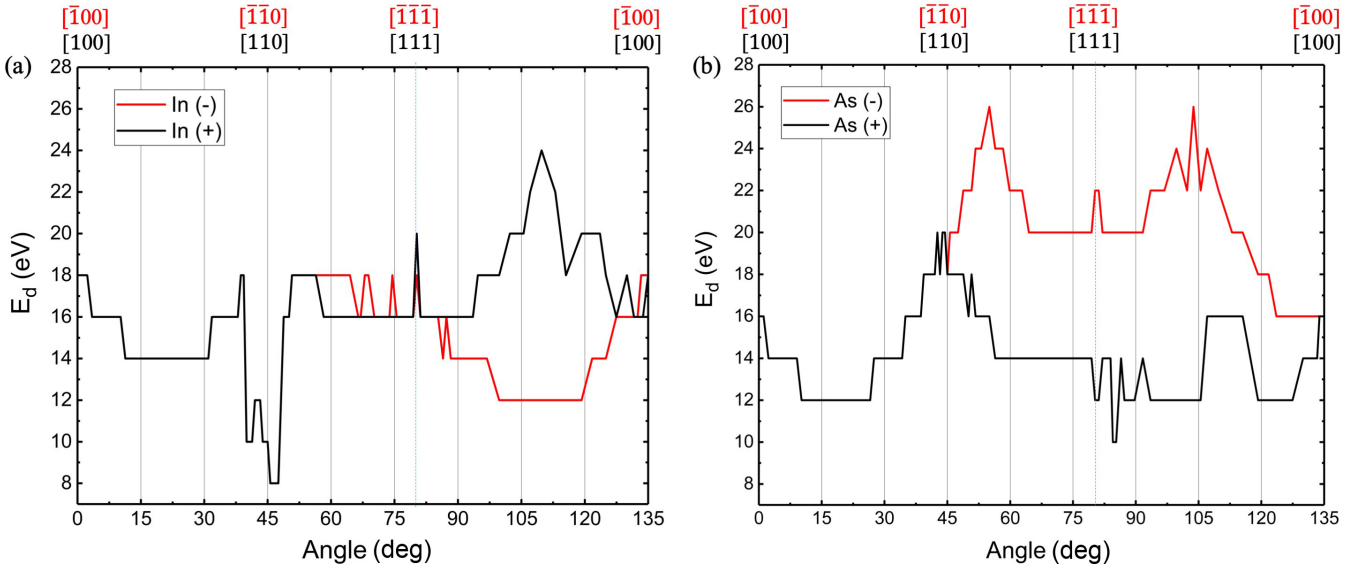

FIG. 2. The displacement threshold energy around the sides of the unit stereographic triangles for (a) In and (b) As atoms.

As atoms. The distribution of the energy levels somewhat matches each other, except that an As atom requires 2 eV more than an In atom at the highest E_d. That is because for both In and As atoms, the strongest repulsive energy comes from another atom species in a comparable environment. The first nearest neighbor atom encountered or bypassed in that direction is just 2.62 Å apart. The highest value of 26 eV is found for As atoms, while a maximum of 24 eV appears for In atoms, which occurs to trigger the recoil events located in the vicinity of the stereographic projection triangle sides. This is quite different from what occurs in GaAs, in which the central part of the triangle corresponds to a higher kinetic energy. For convenience, an overview of the quantitative results including some special low-index directions is summarized in Table I. Experimentally, the lowest threshold energy was estimated to be 6.7 eV for In and 8.5 eV for As atoms [38], and a measured value of 7.4 eV was reported by Johnston [39]. The coincidence of our prediction of 8 eV as the minimum for both species with the established data indicates a satisfactory agreement. Statistically, by averaging the threshold energy over thousands of directions, we obtain a solid value of 15.3 eV for In and 15.8 eV for As atoms after combining both positive and negative directions, which is recommended for the input to radiation damage calculations. The slightly higher value for As is expected due to the fact of size discrepancy, which is consistent with the observation by Vavilov and Ukhin [38].

B. Cascade morphology and defect generation

In light of the comprehensive study of threshold displacement, simulations have been carried out to explore the nature of damage produced by incident energetic atomic particles. It is known that the displacement cascade in semiconductors

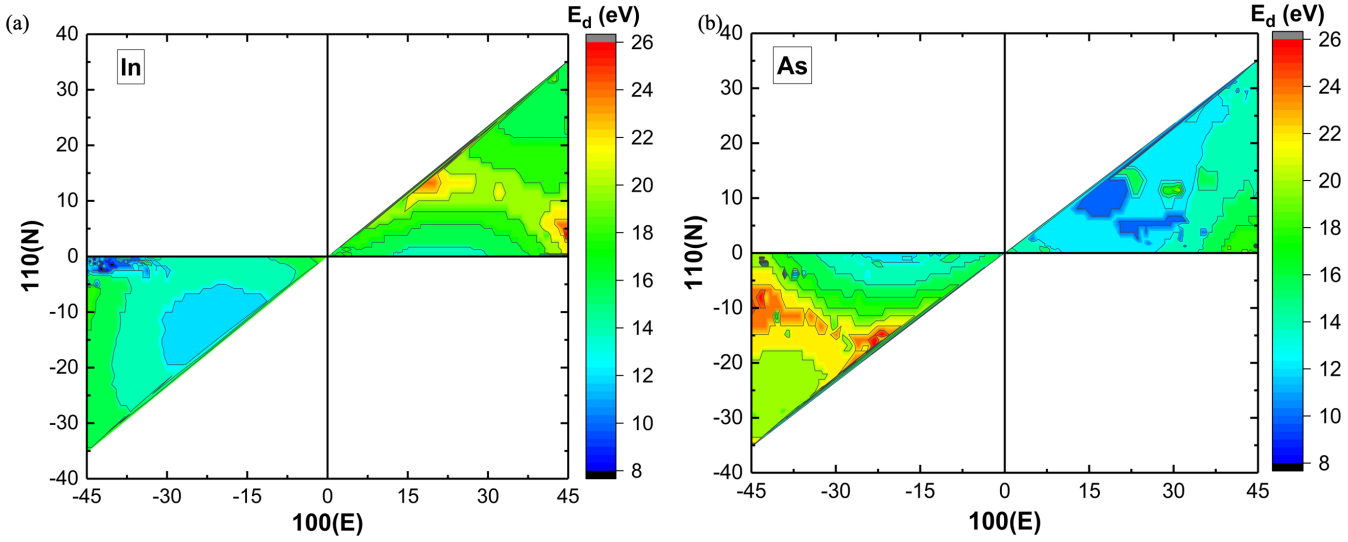

FIG. 3. Threshold energy map for (a) In and (b) As atoms.

TABLE I. Overview of displacement energies compared with experimental data. E_d^{ave} stands for average displacement energy over 3000 directions for each type; $N_{direction}$ is the number of directions simulated for each species.

					E_d (eV)						
	$N_{direction}$	E_d^{ave} (eV)	E_d^{min} (eV)	E_d^{max} (eV)	[100]	[$\bar{1}$00]	[110]	[$\bar{1}\bar{1}$0]	[111]	[$\bar{1}\bar{1}\bar{1}$]	Experiment
In	1828	15.3	8	24	18	18	10	10	10	18	6.7 (In)[a] 8.5 (As)[a]
As	1828	15.8	8	26	16	16	18	18	12	22	7.4[b]

[a]Reference [38].
[b]Reference [39].

exhibits two basic phases, including a collisional phase and a recombination phase afterwards. The first phase can last a few tenths of a picosecond (ps), during which the primary recoil atom will initiate an avalanche of atomic displacements, resulting in many displaced atoms away from their lattice sites. After the number of displacements reaches a maximum, i.e., peak damage, the system tends to cool down and the second phase follows. At about 10 ps, the system becomes stabilized; i.e., no significant defect migration takes place. The simulated peak and final damage of a typical 20 keV cascade in InAs are displayed in Figs. 4(a) and 4(b), respectively, where different defects are represented by the size and color as indicated in the legend. The 20 keV In recoil is initiated at the left side of the MD box followed by a rapid buildup in the number of displaced atoms during the collisional phase. At about 1.13 ps, the 20 keV cascade damage by In PKA reaches a peak and generates a high density of defects. The peak damage is mitigated by the recombination phase as generated interstitials and vacancies are migrating in the sample. Unlike the cascade morphology in GaN [12], InAs creates multiple damage domains along the path of the PKA, resulting in several subcascades. This feature resembles what has been observed in GaAs [11] and SiC [40]. The distribution of the final damage of a 20 keV cascade in Fig. 4(b) looks similar to that of the peak damage, except that a certain number of displaced atoms recombines locally with vacancies, leading to roughly 63% of recombination compared with Fig. 4(a). The surviving defects are mostly in the form of clusters, thus creating distinct disordered regions rather than single interstitials and monovacancies, which are prevalent in GaAs and SiC as well.

To characterize the evolution and nature of these cascades, the number of displaced atoms and antisite defects in InAs for a 20 keV cascade are plotted in Figs. 5(a) and 5(b) as a function of time, in comparisons with those in GaAs and GaN. It is obvious that the number of displaced atoms N_d for all three materials increases up to a damage peak, followed by a decrease during the recombination phase. However, the decrease in the three materials is at various levels, where a 63% recombination was realized in InAs, 18% in GaAs, and 96% in GaN. The antisite defects seen in Fig. 5(b) share the same feature for all three compound semiconductors in which the generation of antisite defects occurs during the collisional phase. A decrease in the number of antisite defects takes place during the recombination phase, attributed to short replacement-collision sequences. However, the slow recovery of antisite defects was observed for both InAs and GaAs, which may be prohibited by the formation of amorphous

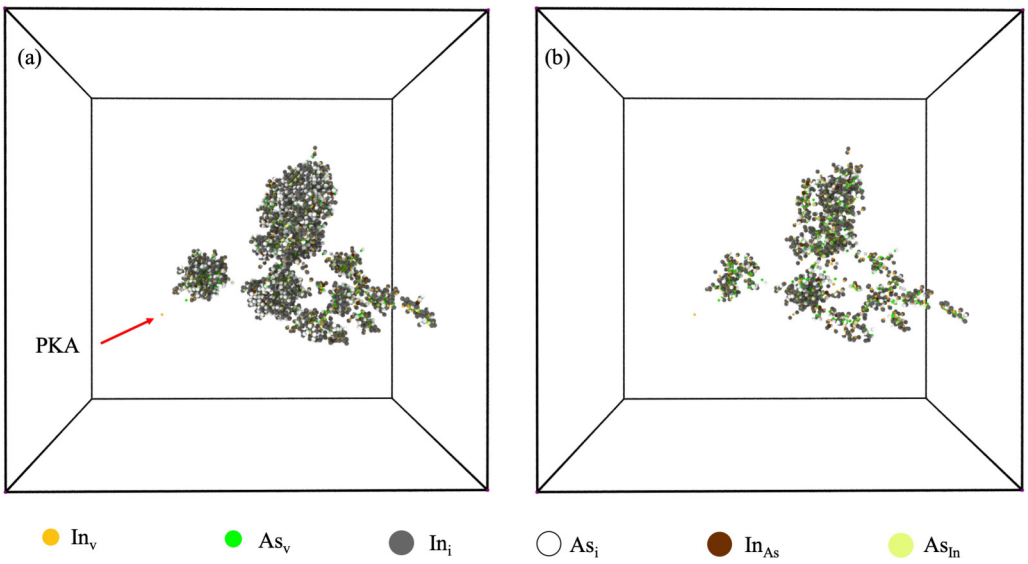

FIG. 4. Two snapshots of a typical 20 keV cascade generated by an In PKA in InAs exhibiting (a) peak damage at 1.13 ps and (b) final damage state at 20 ps, where only defects are displayed. As indicated, various types of defects are represented by spheres with different sizes and colors.

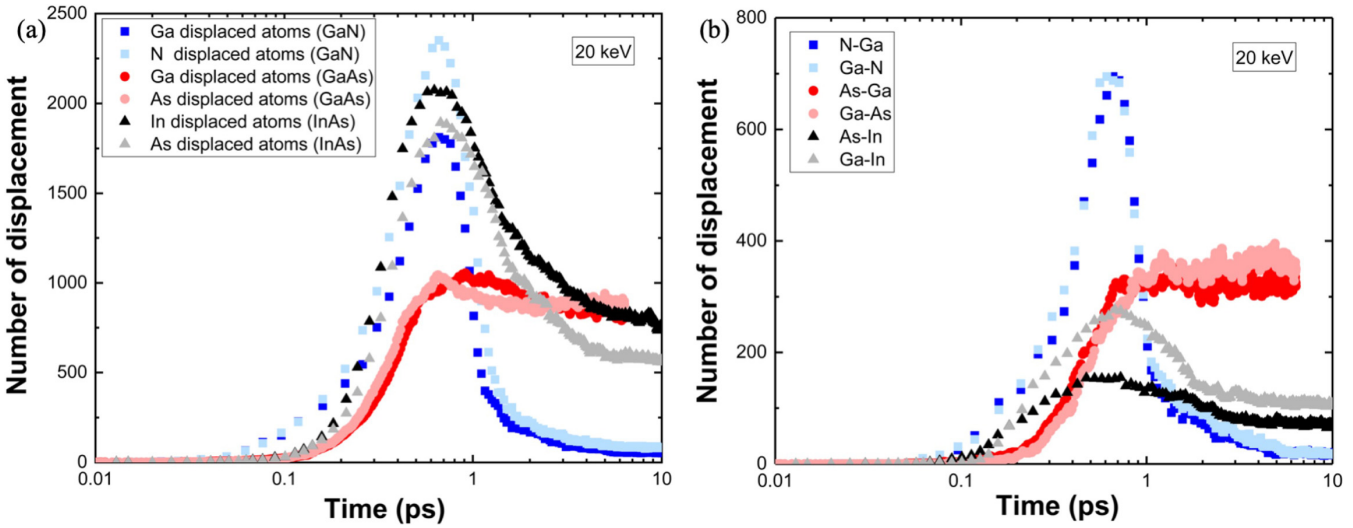

FIG. 5. Comparisons of (a) number of displaced atoms and (b) antisite defects, as a function of time for two 20 keV cascades in GaAs [11], GaN [12], and InAs, respectively.

domains during a cascade. It is known that a cascade lifetime is the period of time beyond which the variation in final number of defects can be neglected. The generated defects are quenched quickly during this time period and form a number of disordered regions. This is, however, different from the phenomenon seen in GaN, in which interstitials are quenched and recombine with nearby vacancies. GaN has a much higher melting temperature (2773 K) than that of InAs (1215 K), which causes the recrystallization front due to a thermal spike moving fast and leads to a smaller fraction of vacancy clusters. Actually, the lower melting point of InAs makes it possible for the heat spikes in InAs to be a bit stronger than those in GaN, which explains why the number of surviving displacements is larger in the former. The mechanism associated with amorphization was proposed earlier by several models [41] due to ion irradiation [42], including direct-impact amorphization. The striking feature in InAs with multiple amorphous domains reveals the occurrence of direct-impact amorphization. Another interesting phenomenon is that the generated defect numbers for In and As atoms appear comparable to each other. This could be attributed to similar average displacement energies for In and As atoms, i.e., 15.3 eV for In and 15.8 eV for As atoms, as calculated in the first section.

Detailed cascade morphologies at the final stable states for 2, 10, and 40 keV cascades by In PKAs can be found from Fig. 6. It was shown in Fig. 4 that a 20 keV In PKA would evolve multiple and separated disordered regions in the cascade. These sub-branches of the cascade along the In PKA path show up when the PKA kinetic energy exceeds 2 keV, as seen in Fig. 6. Below this energy threshold, however, only a single cascade forms with single interstitials and vacancies dominant. At higher incident energies, i.e., 10, 20, and 40 keV, on the other hand, distinct domains are found from Figs. 6(b) and 6(c) for 10 and 40 keV, respectively, and from Fig. 4 for 20 keV even after the completion of an annihilation process of interstitials with vacancies. Here, each domain acquires its

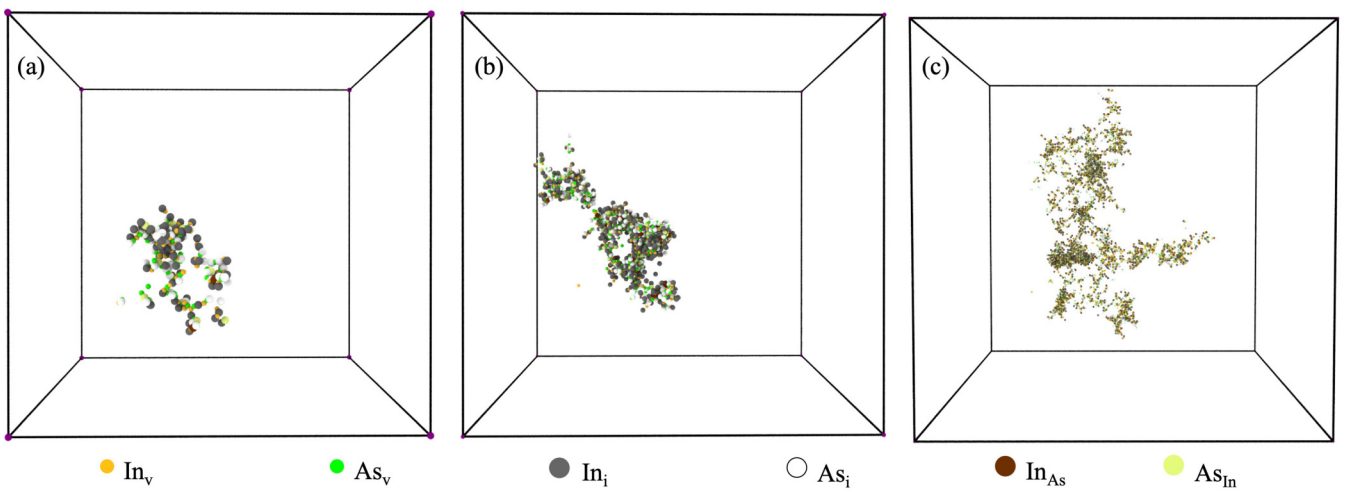

FIG. 6. The final-state defect distributions of a (a) 2, (b) 10, and (c) 40 keV cascade in InAs, from which the transition from a single pocket of atomic displacements to multiple subcascades has been seen.

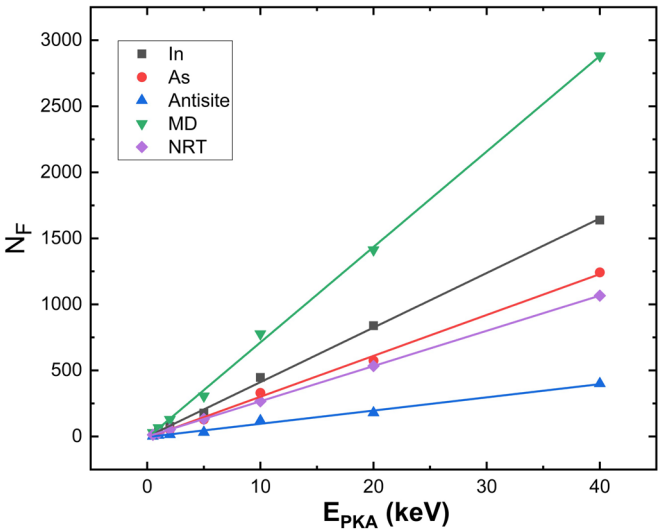

FIG. 7. Number of surviving defects in cascades as a function of PKA energy, where calculated In and As interstitials, as well as antisite defects, are shown separately, along with the NRT values and summation of Frenkel pairs from MD simulations for comparison.

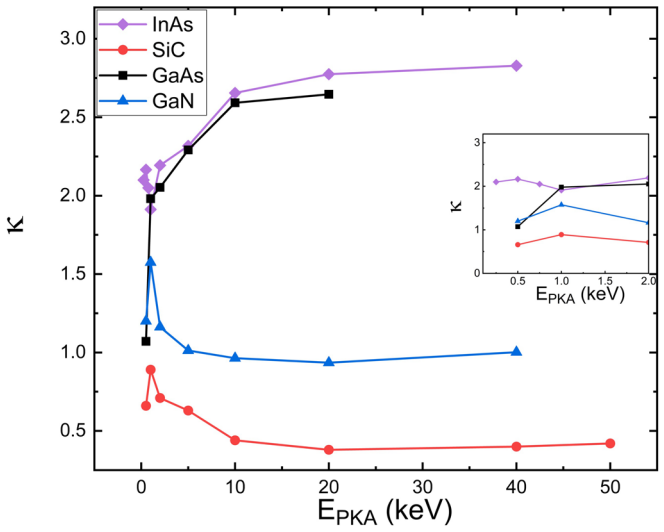

FIG. 8. Defect production efficiencies as a function of cascade energy for InAs, SiC [44], GaAs [11], and GaN [12], respectively.

own core of high defect density. This may result in a nonlinear dependence in defect production due to the formation of these subcascades, which has been shown to be an important factor affecting the NIEL.

As mentioned previously, the final number of defects that survived from displacement cascades is a critical term to study the radiation damage evolution. A standard formula used for estimating the final number of defects from a displacement cascade can be applied for the purpose of a comparison with outcomes of MD simulations to understand defect generation quantitatively. Here, the NRT formula by Norgett *et al.* [43] was used, which can be defined by

$$N_{\mathrm{NRT}} = 0.8E_{\mathrm{PKA}}/2E_d, \tag{16}$$

where N_{NRT} is the value of N_F in the Norgett, Robinson, and Torrens (NRT) formula and E_d stands for the threshold displacement energy averaged over all crystallographic directions. Here, we will adopt a threshold displacement energy of 15 eV calculated in the first part of this section over thousands of directions for InAs. The number of surviving defects from the current MD simulations as a function of PKA energy is presented in Fig. 7, in comparison with the NRT model. In fact, the defect production by the NRT model is not identical to the calculation from MD simulations, as shown in Fig. 7 and the actual N_F is about 2 times higher than N_{NRT} for a given recoil energy E_{PKA}. Especially at high energies, the discrepancy of the NRT model becomes even more severe. This is attributed to the direct-impact amorphization which is absent in the NRT model. The MD simulations, however, uniquely include many-body interaction between a PKA and all lattice atoms in both collisional and recombination phases. This ensures an accurate prediction of the defect production and spatial distribution in cascades.

Another important parameter for characterizing defect production is the defect production efficiency. It utilizes the ratio of N_F to N_{NRT} to quantify the surviving probability of generated defects in target materials. In Fig. 8, the surviving ratio, $\kappa = N_F/N_{\mathrm{NRT}}$, is plotted as a function of the PKA energy with GaAs [11], GaN [12], and SiC [44] imposed for a comparison. It is of interest to note that when the PKA energy increases, the corresponding κ values become more and more distinct. Moreover, it is evident that GaAs and InAs share the same trend, but GaN and SiC exhibit an opposite one. The surviving probabilities for GaAs and InAs increase with PKA energy, where the ratio below 1 keV is provided in the inset graph of Fig. 8 with some fluctuations for InAs. The ratio for InAs changes most for PKA energies ranging from 1 to 20 keV, which can be referred to as a nonlinear region. Such distinctive nonlinear behavior can be explained by the direct-impact amorphization because the formation of these disordered regions will be exaggerated at higher energies for both InAs and GaAs. However, κ decreases rapidly for GaN and SiC once recombination becomes significant. Interestingly, we find a slight increase of κ at high PKA energies (>20 keV) for both GaN and SiC, where subcascades start but do not result in direct-impact amorphization. In fact, these high-energy cascades tend to dissociate into multiple low-energy cascades, leading to a small increase of κ.

C. Effective NIEL

NIEL is a valuable tool and can be employed for scaling damage produced by different particles or for simulating the complex space environment using ground experiments. To calculate the effective NIEL, we have to introduce the number of Frenkel pairs, N_F^{MD}, calculated directly from MD simulations for a certain energy range to extrapolate the values into the high-energy regime. As proposed previously [45] the number of Frenkel pairs displays a power-law dependence on PKA energy E_{PKA}. The energy density deposited by a PKA is equal to $\rho = E_{\mathrm{PKA}}/N_{pk}$ based on the assumption that energy transfer occurs just before the peak damage with a maximum value N_{pk} for the number of produced Frenkel pairs at a given PKA energy. As a result, we can write down the following

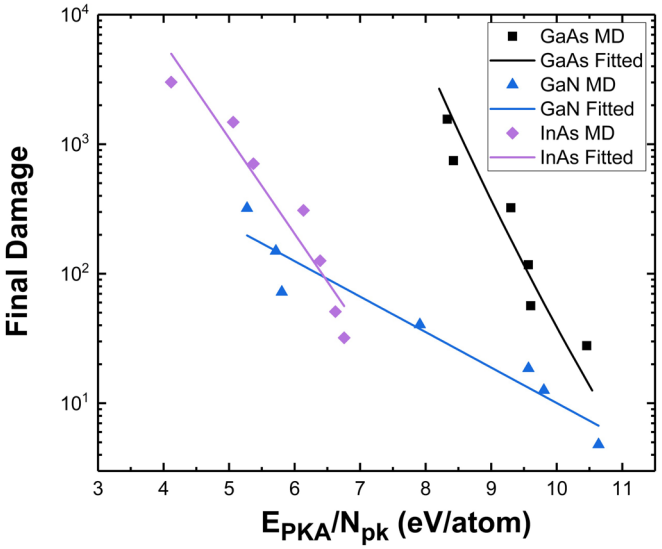

FIG. 9. Final damage number (interstitials) as a function of energy density deposited by a PKA in InAs, where the solid lines represent the fits to MD data. The corresponding results for GaAs [11] and GaN [12] are also presented for comparison.

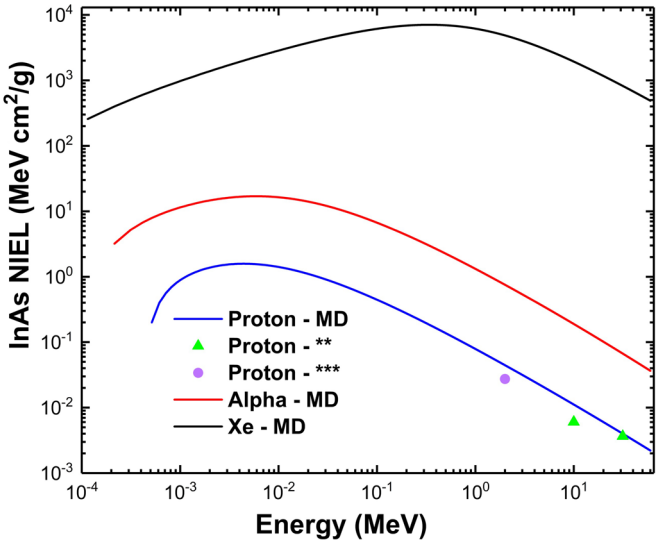

FIG. 10. Calculated NIEL based on the MD simulation results with respect to the energy density deposited by a PKA (protons, alpha, and Xe particles) in InAs (** from Ref. [46] and *** from Ref. [47]).

data correlation,

$$N_F^{\mathrm{MD}} = A(E_{\mathrm{PKA}})^n \rho^m, \tag{17}$$

where A and m are constants to be estimated by fitting to the number density obtained from MD simulations, while n is a dimensionless parameter. These three parameters for InAs are approximately equal to 128.7922, 1.0222, and −0.41, respectively. Since ρ is calculated by E_{PKA}/N_{pk}, the relation between N_F^{MD} and ρ data is presented in Fig. 9, where lines represent the correlated values based on Eq. (17). It is obvious that the final damage decreases with increasing energy density. This is because a large number of defects generated in the high-energy regime reduces the energy density.

The result estimated by MD simulation in Fig. 9 also demonstrates a good match with the analytical power model proposed earlier. This is an indication of the applicability of MD calculated data to evaluating the effective NIEL of InAs. Traditionally, NIEL is useful for comparing damaging effects in the same semiconductor material with different incident particle species. In the current work, proton, alpha, and Xe particles are chosen to test damage in InAs, where the corresponding NIEL results are presented in Fig. 10 including data from the literature. The general tendency for various particles is quite similar, i.e., an increasing NIEL with incident particle energy until a maximum is reached, and then followed by a decreasing NIEL in the high-energy regime. The energy corresponding to the peak NIEL depends on the mass of the incident particles. The heavier the incident particle, the larger the kinetic energy required to reach the maximum NIEL. Such behavior is universal for compound semiconductors, such as GaAs [11] and GaN [12]. As shown in Fig. 10, the magnitude of NIEL values also displays a strong dependence on incident particle species, having the highest NIEL for Xe particles. Even though there is a lack of data for both alpha and Xe particles from the literature, our predicted NIEL for protons is comparable with experimentally measured ones with proton irradiation at several energies [46,47]. This provides a validation of our model in predicting NIEL for incident protons with energies up to 60 MeV.

To highlight the difference in NIELs between InAs and several other compound semiconductors, the NIEL ratios for both InAs to GaN and InAs to GaAs are plotted in Figs. 11(a) and 11(b), respectively. The effective NIEL of InAs for protons in Fig. 11(a) is always larger than that of GaN. The lowest ratio for protons is found to be 1.30 at 2.85 keV, while the lowest ratio for alpha particles drops to 0.80 at 950 eV. As a heavy ion Xe is introduced around 450 eV, the NIEL ratio to GaN becomes 0.83. The minimum NIEL ratios for alpha and Xe particles are almost the same, but at different energetic levels. At energies above 4.65 keV, the NIEL of InAs is greater than that of GaN for high particle energies, implying a better resilience of GaN in a space radiation environment. For low incident particle energies, however, this ratio becomes slightly below 1 for incident alpha and Xe particles. This might set InAs as a preferable material to resist radiation damage in this energy range for Xe and alpha particles in comparison with GaN. Also interesting is the NIEL ratio of InAs to GaAs, which is found close to unity in Fig. 11(b) in the high-energy regime. This is understandable by considering the similarities found for both cascade morphology and nonlinear effect in InAs and GaAs. However, the actual value of this ratio is still below 1 for all energies, which might limit the use of GaAs based devices in a space radiation environment, where the damaging effects would be higher in GaAs compared to that in InAs. Therefore, the excellent optoelectronic performance of InAs can promote it to becoming a potential candidate for space applications. As seen from both InAs to GaN and InAs to GaAs ratios, as well as from a comparative study of the GaN to GaAs ratio published previously [48], we conclude that the most radiation resistant material of the three is GaN,

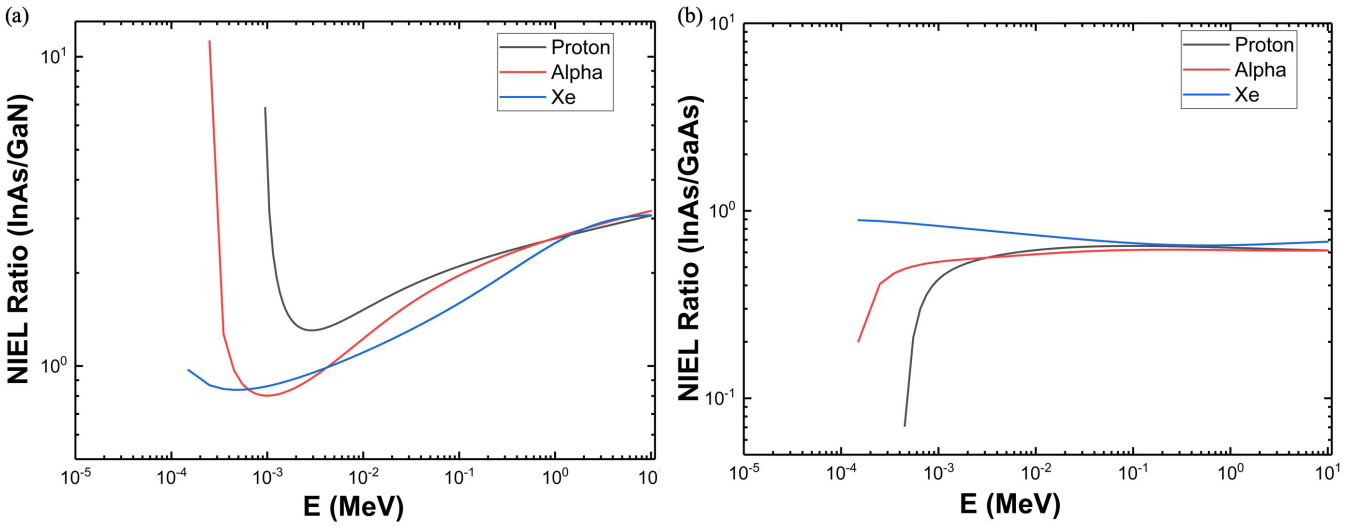

FIG. 11. NIEL ratio for (a) InAs to GaN and (b) InAs to GaAs irradiated by proton, alpha, and Xe particles.

which is thus most suitable for high-power space applications, especially in the high-energy regime.

IV. CONCLUSION

In this paper, a molecular dynamics method has been employed to determine the threshold displacement energies for In and As atoms with a set of bond-order potential parameters describing the interaction between In and As. The results have demonstrated a weak dependence on the crystallographic direction along which an atom is displaced. Different types of lattice-atom vibrational modes and atomic sizes are believed to be responsible for this observed dependence. The minimum E_d for both In and As atoms is found to be in satisfactory agreement with the available experimental data. The threshold displacement energy, averaged over 3600 directions for each species, is 15 eV, which can be applied to determine defect generation in the theory of radiation damage. Defect production and its detailed evolution in InAs were then studied for PKA energies ranging from 500 eV to 40 keV. The direct-impact amorphization becomes significant in the high-energy regime, giving rise to multiple disordered pockets similar to those in GaAs. A nonlinear defect production, which starts to build up at 1 keV, is an important factor in developing the effective NIEL model. Based on the MD simulation results, the calculated NIEL for proton irradiation has closely reproduced the experimental data at several energies, which shows the reliability of our current model even though more supportive data are still needed. Additionally, by comparing NIELs for different semiconductors, we have found the limitation of GaAs in sustaining the displacement damage induced by space radiation, while both InAs and GaN have proven themselves as more immune to radiation damage than GaAs in all energy ranges. The calculated NIEL ratio has confirmed GaN to be the best candidate of the three as a radiation hard material for space applications in the high-energy regime, where the defect production by irradiation in GaN is quite rare. For low incident particle energies at which the NIEL ratio of InAs to GaN is less than 1, the performance of InAs may be superior to that of GaN for space applications.

ACKNOWLEDGMENTS

This research was supported by Contract No. FA9453-17-2-0010 of the Air Force Research Laboratory (AFRL). D.H. would like to thank the Air Force Office of Scientific Research (AFOSR) for support.

[1] O. Madelung, *Semiconductors: Group IV Elements and III-V Compounds* (Springer, Berlin, Heidelberg, 1991).

[2] R. E. Nahory, M. A. Pollack, W. D. Johnston, and R. L. Barns, Band gap versus composition and demonstration of Vegard's law for $In_{1-x}Ga_xAs_yP_{1-y}$ lattice matched to InP, Appl. Phys. Lett. **33**, 659 (1978).

[3] D. Richards, J. Wagner, and J. Schmitz, Landau damped intersubband plasmons in InAsAlSb quantum wells, Solid State Commun. **100**, 7 (1996).

[4] L. Balaghi, G. Bussone, R. Grifone, R. Hübner, J. Grenzer, M. Ghorbani-Asl, A. V. Krasheninnikov, H. Schneider, M. Helm, and E. Dimakis, Widely tunable GaAs bandgap via strain engineering in core/shell nanowires with large lattice mismatch, Nat. Commun. **10**, 2793 (2019).

[5] G. Satyanadh, R. P. Joshi, N. Abedin, and U. Singh, Monte Carlo calculation of electron drift characteristics and avalanche noise in bulk InAs, J. Appl. Phys. **91**, 1331 (2002).

[6] B. D. Weaver, T. J. Anderson, A. D. Koehler, J. D. Greenlee, J. K. Hite, D. I. Shahin, F. J. Kub, and K. D. Hobart, On the Radiation Tolerance of AlGaN/GaN HEMTs, ECS J. Solid State Sci. Technol. **5**, Q208 (2016).

[7] S. R. Messenger, E. A. Burke, M. A. Xapsos, G. P. Summers, R. J. Walters, I. Jun, and T. Jordan, Niel for heavy ions: an analytical approach, IEEE Trans. Nucl. Sci. **50**, 1919 (2003).

[8] S. R. Messenger, M. A. Xapsos, E. A. Burke, R. J. Walters, and G. P. Summers, Proton displacement damage and ionizing dose for shielded devices in space, IEEE Trans. Nucl. Sci. **44**, 2169 (1997).

[9] S. M. Khanna, D. Estan, L. S. Erhardt, A. Houdayer, C. Carlone, A. Ionascut-Nedelcescu, S. R. Messenger, R. J. Walters, G. P. Summers, J. H. Warner, and I. Jun, Proton energy dependence of the light output in gallium nitride light-emitting diodes, IEEE Trans. Nucl. Sci. **51**, 2729 (2004).

[10] J. Ziegler, J. Biersack, and U. Littmark, *Stopping and Range of Ions in Solids* (Pergamon Press, New York, 1985), Vol. 1.

[11] F. Gao, N. Chen, E. Hernandez-Rivera, D. Huang, and P. D. LeVan, Displacement damage and predicted non-ionizing energy loss in GaAs, J. Appl. Phys. **121**, 095104 (2017).

[12] N. Chen, E. Rasch, D. Huang, E. R. Heller, and F. Gao, Atomic-Scale Simulation for Pseudometallic Defect-Generation Kinetics and Effective NIEL in GaN, IEEE Trans. Nucl. Sci. **65**, 1108 (2018).

[13] C. Inguimbert, P. Arnolda, T. Nuns, and G. Rolland, "Effective NIEL" in Silicon: Calculation Using Molecular Dynamics Simulation Results, IEEE Trans. Nucl. Sci. **57**, 1915 (2010).

[14] M. W. Finnis, MOLDY6-A Molecular Dynamics Program for Simulation of Pure Metals (AERE-R–13182) (UKAEA Harwell Lab. Theoretical Physics Div, 1988).

[15] A. F. Calder and D. J. Bacon, A molecular dynamics study of displacement cascades in α-iron, J. Nucl. Mater. **207**, 25 (1993).

[16] F. Gao, D. J. Bacon, P. E. J. Flewitt, and T. A. Lewis, A molecular dynamics study of temperature effects on defect production by displacement cascades in α-iron, J. Nucl. Mater. **249**, 77 (1997).

[17] E. Wigner and F. Seitz, On the Constitution of Metallic Sodium, Phys. Rev. **43**, 804 (1933).

[18] K. Nordlund, M. Ghaly, and R. S. Averback, M. Caturla, T. Diaz de la Rubia, and J. Tarus, Defect production in collision cascades in elemental semiconductors and fcc metals, Phys. Rev. B **57**, 7556 (1998).

[19] J. B. Gibson, A. N. Goland, M. Milgram, and G. H. Vineyard, Dynamics of radiation damage, Phys. Rev. **120**, 1229 (1960).

[20] S. M. Foiles, Detailed characterization of defect production in molecular dynamics simulations of cascades in Si, Nucl. Instrum. Methods Phys. Res., Sect. B **255**, 101 (2007).

[21] K. Albe, K. Nordlund, J. Nord, and A. Kuronen, Modeling of compound semiconductors: Analytical bond-order potential for Ga, As, and GaAs, Phys. Rev. B **66**, 035205 (2002).

[22] K. Albe, K. Nordlund, and R. S. Averback, Modeling the metal-semiconductor interaction: Analytical bond-order potential for platinum-carbon, Phys. Rev. B **65**, 195124 (2002).

[23] T. Hammerschmidt, P. Kratzer, and M. Scheffler, Analytic many-body potential for InAs/GaAs surfaces and nanostructures: Formation energy of InAs quantum dots, Phys. Rev. B **77**, 235303 (2008).

[24] S. T. Murphy, A. Chroneos, R. W. Grimes, C. Jiang, and U. Schwingenschlögl, Phase stability and the arsenic vacancy defect in In x $Ga_{1-x}As$, Phys. Rev. B **84**, 184108 (2011).

[25] A. Höglund, C. W. M. Castleton, M. Göthelid, B. Johansson, and S. Mirbt, Point defects on the (110) surfaces of InP, InAs, and InSb : A comparison with bulk, Phys. Rev. B **74**, 075332 (2006).

[26] P. A. Schultz, Simple Intrinsic Defects in InAs: Numerical Predictions, Sandia Report No. SAND2013-2477, 2013.

[27] See Supplemental Material at http://link.aps.org/supplemental/10.1103/PhysRevMaterials.5.033603 for more information about the interatomic potential fitting process as well as the potential parameter sets used in the simulation. Comparisons of bulk properties, and defect formation energies with experiment and theory are also included.

[28] Y. A. Burenkov, S. Y. Davydov, and S. P. Nikanorov, Elastic properties of indium arsenide, Fiz. Tverd. Tela **17**, 2183 (1975).

[29] S. Plimpton, Fast parallel algorithms for short-range molecular dynamics, J. Comput. Phys. **117**, 1 (1995).

[30] D. W. Marquardt, An Algorithm for Least-Squares Estimation of Nonlinear Parameters, J. Soc. Ind. Appl. Math. **11**, 431 (1963).

[31] L.-F. Wang, X. Shu, G.-H. Lu, and F. Gao, Embedded-atom method potential for modeling hydrogen and hydrogen-defect interaction in tungsten, J. Phys.: Condens. Matter **29**, 435401 (2017).

[32] J. P. Biersack and J. F. Ziegler, Refined universal potentials in atomic collisions, Nucl. Instrum. Methods, Phys. Res. **194**, 93 (1982).

[33] Y. J. Lindhard, M. Scharff, H. E. Schiøt, and T. København, Range concepts and heavy ion ranges (notes on atomic collisions II) Mat. - Fys. Medd. - K. Dan. Vidensk Selsk. **3**, 4 (1963).

[34] C. Erginsoy, G. H. Vineyard, and A. Englert, Dynamics of radiation damage in a body-centered cubic lattice, Phys. Rev. **133**, A595 (1964).

[35] N. Chen, S. Gray, E. Hernandez-Rivera, D. Huang, P. D. LeVan, and F. Gao, Computational simulation of threshold displacement energies of GaAs, J. Mater. Res. **32**, 1555 (2017).

[36] E. Holmström, A. Kuronen, and K. Nordlund, Threshold defect production in silicon determined by density functional theory molecular dynamics simulations, Phys. Rev. B **78**, 045202 (2008).

[37] S. Ghaderzadeh, M. Ghorbani-Asl, S. Kretschmer, G. Hlawacek, and A. V. Krasheninnikov, Channeling effects in gold nanoclusters under He ion irradiation: Insights from molecular dynamics simulations, Nanotechnology **31**, 035302 (2020).

[38] V. S. Vavilov and N. A. Ukhin, *Radiation Effects in Semiconductors and Semiconductor Devices* (Springer US, Boston, MA, 1995).

[39] A. H. Johnston, *Reliability and Radiation Effects in Compound Semiconductors* (World Scientific, Singapore, 2010).

[40] F. Gao and W. J. Weber, Atomic-scale simulation of 50 keV Si displacement cascades in β-SiC,, Phys. Rev. B **63**, 054101 (2000).

[41] W. Weber, Models and mechanisms of irradiation-induced amorphization in ceramics, Nucl. Instrum. Methods Phys. Res., Sect. B **166–167**, 98 (2000).

[42] M. Nastasi, J. Mayer, and J. K. Hirvonen, and M. James, *Ion-Solid Interactions: Fundamentals and Applications*, Cambridge Solid State Science Series (Cambridge University Press, Cambridge, 1996).

[43] M. J. Norgett, M. T. Robinson, and I. M. Torrens, A proposed method of calculating displacement dose rates, Nucl. Eng. Des. **33**, 50 (1975).

[44] F. Gao, W. Weber, and R. Devanathan, Atomic-scale simulation of displacement cascades and amorphization in β-SiC, Nucl. Instrum. Methods Phys. Res., Sect. B **180**, 176 (2001).

[45] D. J. Bacon, A. F. Calder, F. Gao, V. G. Kapinos, and S. J. Wooding, Computer simulation of defect production by displacement cascades in metals, Nucl. Inst. Methods Phys. Res., Sect. B **102**, 37 (1995).

[46] X. Zhou, B. White, X. Meng, S. Zhang, M. Gutierrez, M. Robbins, L. G. Rojas, N. Nelms, C. H. Tan, and J. S. Ng, Proton radiation effect on InAs avalanche photodiodes, Opt. Express **25**, 2818 (2017).

[47] J. H. Warner, D. McMorrow, S. Buchner, J. B. Boos, N. Roche, P. Paillet, M. Gaillardin, E. Blackmore, M. Trinczek, V. Ramachandran, R. A. Reed, and R. D. Schrimpf, Proton-Induced Transient Charge Collection in GaAs and InAlSb/InAs-Based FETs, IEEE Trans. Nucl. Sci. **60**, 2651 (2013).

[48] F. Gao, N. Chen, D. Huang, E. R. Heller, and P. D. LeVan, Atomic-level based non-ionizing energy loss: an application to GaAs and GaN semiconductor materials, in *Infrared Sensors, Devices, and Applications VIII*, edited by P. D. LeVan, P. Wijewarnasuriya, and A. I. D'Souza (SPIE, Bellingham, WA, 2018), p. 3.